

1 **Statistical investigations of the flow-aligned component of IMF impact on current**
2 **sheet structure in the Martian magnetotail: MAVEN observations**

3
4 **Yuanzheng Wen^{1,2}, Zhaojin Rong^{2,3}, Hans Nilsson⁴, Chi Zhang^{2,3}, Mats Holmstrom⁴, Dan**
5 **Tao¹, Guangxue Wang¹, Yiteng Zhang⁵, Jasper Halekas⁶, Jared Espley⁷**

6
7 ¹School of Geophysics, Chengdu University of Technology, Chengdu, China.

8 ²Key Laboratory of Earth and Planetary Physics, Institute of Geology and Geophysics, Chinese
9 Academy of Sciences, Beijing, China.

10 ³College of Earth and Planetary Sciences, University of Chinese Academy of Sciences, Beijing,
11 China.

12 ⁴Swedish Institute of Space Physics, Kiruna, Sweden.

13 ⁵National Space Science Center, Chinese Academy of Sciences, Beijing, China.

14 ⁶Department of Physics and Astronomy, University of Iowa, Iowa City, USA.

15 ⁷NASA Goddard Space Flight Center, Greenbelt, USA.

16
17 Corresponding author: Zhaojin Rong (rongzhaojin@mail.iggcas.ac.cn)

18
19 **Key Points:**

- 20 • There is a systematic Y (i.e., dawn-dusk) asymmetry in the location of the Martian
21 magnetotail current sheet in the modified MSE coordinates
- 22 • The asymmetry is controlled by the flow-aligned component of IMF, shifting to the dawn
23 (-Y) during the tailward IMF conditions and to the dusk (+Y) during the sunward IMF
24 conditions
- 25 • The shift found in this study is mostly dominated by the IMF, with minor contributions
26 from the crustal magnetic fields and solar EUV intensity.

27 **Abstract**

28 In this study, we investigated the role of IMF orientation at controlling the location and structure
29 of the current sheet in the Martian magnetotail. Here based on carefully selected cases as well as
30 statistical studies by using the magnetic field data of MAVEN MAG from October 2014 to
31 February 2020, our study shows the IMF orientation can systematically influence the magnetotail
32 current sheet structure of Mars. It is found that significantly tailward IMF conditions result in a
33 Venus-like magnetotail configuration with the current sheet shifted to the -Y (dawnside) direction.
34 Sunward IMF conditions result in a tail configuration with the current sheet shifted to the +Y
35 (duskside) direction. The lobes follow this pattern, with the current sheet shifting away from the
36 larger lobe. However, the current sheet did not show significant displacement under cross-flow
37 dominant IMF conditions. Moreover, crustal magnetic fields and other factors can also influence
38 the current sheet structure, but the IMF orientation is still the dominant controlling factor from our
39 study. Our results demonstrate that the flow-aligned component of the IMF can influence and
40 systematically control the current sheet structure in the Martian magnetotail.

41 **Plain Language Summary**

42 Mars, which does not have an intrinsic magnetic field, has formed an induced magnetic
43 environment from the draping of the interplanetary magnetic field (IMF) from the Sun. It folds
44 around Mars, forming two “lobes” of magnetic field behind the planet with a current sheet of
45 electrified gas (plasma) behind it. The current sheet is not always directly behind the planet but
46 rather shifted toward the dawn or dusk direction. It is shown in our study that one factor that can
47 control the location of the current sheet is the flow-aligned component of the IMF (B_x). The current
48 sheet is shifted toward dawn (+Y) under sunward IMF condition and shifted dusk (-Y) under the
49 tailward IMF condition, while the current sheet shows little displacement under cross-flow IMF
50 condition.

51

52 **1 Introduction**

53 Mars, like Venus, lacks a strong internal dipole magnetic field, so the solar wind and
54 interplanetary magnetic field impacts directly on Mars’s ionosphere and atmosphere (*Nagy et al.*,
55 [2004]; *Bertucci et al.*, [2011]). The interaction induces ionospheric electric currents in the

56 ionosphere, which causes the IMF to pileup and drape over the planet. This results in the formation
 57 of two magnetic lobes behind the planet, a tail current sheet (CS) is between the two lobe regions
 58 with antiparallel field lines (*Dubinin and Fraenz [2015]*).

59 An earlier study by *McComas et al. [1986]*, found an interesting feature of the magnetotail of
 60 Venus using Pioneer Venus Orbiter (PVO) data from the distant tail, which is that its location to
 61 the planet exhibits a dawn-to-dusk asymmetry. In the statistical study, it was found that the average
 62 location of the CS center is shifted toward the $+B_X$ by $0.5 R_V$. The average magnetic field angle
 63 (computed as $\text{atan}(B_X/B_Y)$) in the lobe of $-B_X$ hemisphere is -78.4° and 73.4° in the lobe of $+B_X$
 64 hemisphere. The lobe transverse width of the $-B_X$ hemisphere and the $+B_X$ hemisphere were
 65 estimated to be $2.1 R_V$. and $1.6 R_V$., respectively. The amplitude of the X component of the
 66 magnetic field in the lobe of $-B_X$ hemisphere was found larger than that in the $+B_X$ hemisphere,
 67 it was suggested that the flow-aligned component of the IMF influences the magnetic field
 68 configuration of the Venusian magnetotail. This shift was confirmed by magnetohydrodynamics
 69 (MHD) calculations of the Venus space environment by *Ma et al. [2013]*. However, by using the
 70 magnetic field data of Venus Express (VEX) from April 2006 to December 2014, along with
 71 carefully selected cases and a statistical study, *Rong et al. [2016]* showed that the exact structure
 72 of the near-Venus magnetotail asymmetry is actually insensitive to the flow-aligned component of
 73 the IMF. The IMF B_X does not significantly impact the magnetic field structure of the current sheet.
 74 From their study, the true reason for the shift still seems to be an open issue.

75 Similarly, the shift has also been observed at Mars and Titan. Simulations by *Simon et al.*
 76 [2009] showed that the flow-aligned component of the IMF can displace the current sheet and
 77 cause the asymmetric structure in the magnetotail of Titan. Moreover, by checking the magnetic
 78 field data of Cassini for 85 flybys of Titan, *Simon et al. [2013]* found a consistent correlation
 79 between the shift of the current sheet and corotation flow component of the background magnetic
 80 field. By using the data from Mars Global Surveyor (MGS), *Halekas et al. [2006]* found many
 81 current sheet crossings in upper ionospheric magnetic data at 2 A.M. local time, implying a
 82 systematic -Y shift in the magnetotail current sheet. In contrast, *DiBraccio et al. [2015]* showed
 83 observations of a satellite pass in the near-Mars tail, demonstrating a shift to the +Y direction for
 84 the magnetic field reversal (the location of the current sheet). Moreover, *Romanelli et al. [2015]*
 85 used magnetometer data from the MGS and checked the distributions of data points in the Martian

86 magnetotail for different polarities of IMF B_x and found a correlation between the IMF and its
87 lobes, their results seem to align with *McComas et al.* [1986]. However, their analysis technique
88 is similar to *McComas et al.* [1986] for Venus. Moreover, in their study there is a lack of the
89 simultaneous measurement for the upstream solar wind and IMF conditions, which are always
90 changing during the time spacecraft spends inside the induced magnetosphere. Thus, we cannot
91 conclude that whether the IMF really influences the current sheet structure in magnetotail of Mars
92 since previous study by *Rong et al.* [2016] suggested IMF B_x cannot influence the current sheet
93 structure in the near-Venus magnetotail. Besides, *Romanelli et al.* [2015] discarded all MAG
94 measurements occurring inside the MPB for which the X_{MSO} coordinate is higher than $-1.5 R_M$ to
95 filter out the potential effects of crustal magnetic fields, while several studies have found
96 systematic influences of the crustal magnetic field locations on the magnetotail configurations [*Ma*
97 *et al.*, 2002; *Harnett and Winglee*, 2005; *Fang et al.*, 2010, 2015; *Dong et al.*, 2015].

98 In this study we investigated the influence of the IMF orientation on the morphology of the
99 current sheet in a much more accurate way based on carefully selected cases along with statistical
100 studies, using MAVEN data from October 2014 to February 2020. Considering the varying
101 upstream solar wind condition, we restricted the study to cases where the upstream IMF variations
102 are as small as possible. Besides, we also considered the effects from the crustal magnetic fields
103 and other factors that may influence the magnetotail configurations, and compared the
104 contributions of these factors. The study is constructed as follows: the instruments and data set
105 applied to this study are briefly introduced in section 2. The analysis technique used to quantitatively
106 evaluate the current sheet structure displacement is presented in section 3. Results from analysis
107 based on selected cases are shown in section 4, while we showed the results from the statistical
108 studies in section 5. In section 6, we summarized our discussions and conclusions.

109 **2 Instrumentation and Data Set**

110 The MAVEN spacecraft was inserted into orbit about Mars on 21 September 2014 and, after
111 a brief commissioning phase, began its primary science investigation on 16 November 2014.
112 MAVEN's 4.5 h elliptical orbit reaches periapsis and apoapsis altitudes of ~ 150 km and ~ 6200
113 km, respectively. The 74° inclination orbit provides global coverage of the Martian space
114 environment, sampling a full range of latitudes and local times over the course of its orbital
115 evolution. [*DiBraccio et al.*, 2017]

116 In this study, the magnetic field, ion and electron data from MAVEN. [Jakosky *et al.*, 2015]
 117 were adopted to identify the current sheet crossing cases. The magnetometer (MAG) [Connerney
 118 *et al.*, 2015] provides vector magnetic field data at a maximum sampling rate of 32 vectors per
 119 second. The Solar Wind Ion Analyzer (SWIA) [Halekas *et al.*, 2013] and Suprathermal and
 120 Thermal Ion Composition (STATIC) [McFadden *et al.*, 2015] instruments measure the flux,
 121 energy, and distributions of ions throughout the Martian space environment at cadences up to 4s.
 122 The Solar Wind Electron Analyzer (SWEA) [D. L. Mitchell *et al.*, 2015] provides electron
 123 distributions as often as once every 2s. MAVEN observations are reported in Mars solar orbital
 124 (MSO) coordinates, unless otherwise stated: X_{MSO} is directed from the center of the planet toward
 125 the Sun, Z_{MSO} is normal to Mars' orbital plane, and Y_{MSO} completes the right-handed system.

126 3 Analysis Technique

127 3.1 The Normal of the Current Sheet

128 The knowledge of the normal to the Current Sheet (CS) is required to study the current sheet
 129 structure in the Martian magnetotail. The minimum variance analysis (MVA) [Sonnerup and
 130 Scheible., 1998] is applied to the MAG data over individual current sheet encounters to determine
 131 the CS normal direction ($\hat{\mathbf{n}}$). Considering the boundary conditions $B_{1n} = B_{2n}$ at the magnetic
 132 discontinuity (because of $\nabla \cdot \mathbf{B} = 0$), where B_{1n} and B_{2n} are the normal components of magnetic
 133 fields at both sides of discontinuity, the normal direction $\hat{\mathbf{n}}$ can be determined by minimization of

$$134 \quad \sigma^2 = \frac{1}{N} \sum_{i=1}^N |(\mathbf{B}_i - \langle \mathbf{B} \rangle) \cdot \hat{\mathbf{n}}|^2 \quad (1)$$

135 Where $\langle \mathbf{B} \rangle = \frac{1}{N} \sum_{i=1}^N \mathbf{B}_i$ and $i=1, 2, 3, \dots, N$. N is the number of data points. With the MVA,
 136 the local Cartesian coordinates, $\{\mathbf{X}_1, \mathbf{X}_2, \mathbf{X}_3\}$, for a CS can be set up. The $\mathbf{X}_1, \mathbf{X}_2, \mathbf{X}_3$ are
 137 orthogonal eigenvectors ($\mathbf{X}_3 = \mathbf{X}_1 \times \mathbf{X}_2$) derived from the magnetic variance matrix $M_{\mu\nu} =$
 138 $\langle B_\mu B_\nu \rangle - \langle B_\mu \rangle \langle B_\nu \rangle$ where the subscripts $\mu, \nu = 1, 2, 3$ denote cartesian components along the X, Y,
 139 Z system. The corresponding eigenvalues for each eigenvector are $\lambda_1, \lambda_2, \lambda_3$ ($\lambda_1 \geq \lambda_2 \geq \lambda_3 \geq 0$).

140 Besides, the angular uncertainty of $\mathbf{X}_1, \mathbf{X}_2, \mathbf{X}_3$ can also be estimated as

$$141 \quad |\Delta\varphi_{ij}| = |\Delta\varphi_{ji}| = \sqrt{\frac{\lambda_3(\lambda_i + \lambda_j - \lambda_3)}{(N-1)(\lambda_i - \lambda_j)^2}} \quad (2)$$

142 Here $|\Delta\phi_{ij}|$ denotes the expected angular uncertainty of eigenvector \mathbf{X}_i for rotation toward or
 143 away from eigenvector \mathbf{X}_j , while N is the number of data points.

144 The eigenvectors $\mathbf{X}_1, \mathbf{X}_2, \mathbf{X}_3$ are usually written as $\hat{\mathbf{L}}, \hat{\mathbf{M}}, \hat{\mathbf{N}}$ to represent the direction of
 145 maximum, intermediate and minimum variance of the magnetic field, respectively. The $\hat{\mathbf{N}}$ here is
 146 regarded as the normal to the CS. The accuracy of MVA results is inferred by the ratio of the
 147 corresponding eigenvalue $\lambda_1, \lambda_2, \lambda_3$. A high intermediate-to-minimum eigenvalue ratio (λ_2/λ_3)
 148 indicates that the normal vector is well determined for a given current sheet crossing. The larger
 149 the ratio is, the more accurate the yielded normal becomes.

150 For further analysis, the normal $\hat{\mathbf{n}}$ is chosen as the vector which always points from $+B_X$ to $-B_X$
 151 hemisphere. Thus, the normal is given by

$$152 \quad \hat{\mathbf{n}} = \text{sgn}(-\Delta B_X) \text{sgn}(\hat{\mathbf{v}}_t \cdot \hat{\mathbf{N}}) \hat{\mathbf{N}} \quad (3)$$

153 Where sgn is the sign function, $\hat{\mathbf{v}}_t$ represents the velocity vector of MAVEN, and $\Delta B_X > 0$, if
 154 B_X change from $-B_X$ to $+B_X$, and vice versa.

155

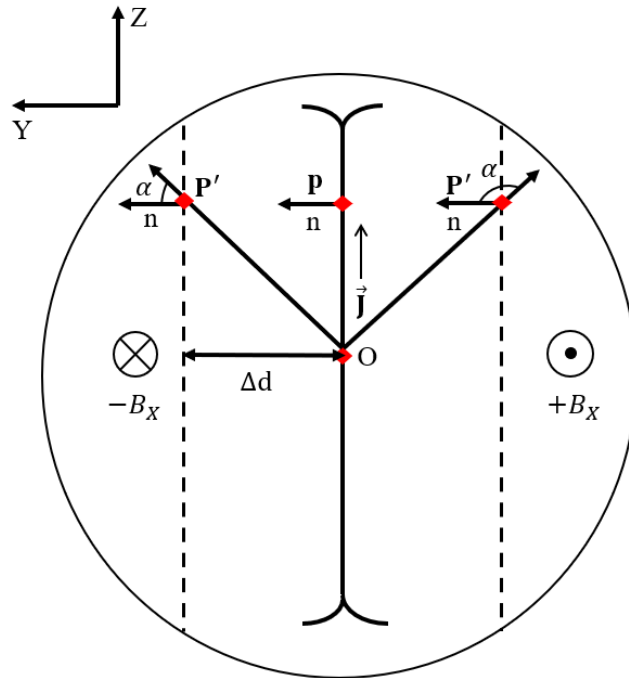
156 3.2 Current Sheet Structure Shift Evaluation

157 To study the correlations between the flow-aligned component of IMF and the CS structure
 158 shift, the shift of the CS must be estimated with the IMF flow-aligned component taken into
 159 account.

160 Here an example method is presented to quantitatively analyze the shift of CS structure. The
 161 CS is ideally assumed to be a plane structure, and the solar wind flow is along the $-X$ direction. As
 162 presented in Figure 1 in the YZ plane, the CS, if no shift occurs (see the thick black line), would
 163 contain the Sun-Mars line, which projected onto the YZ plane is the point O , i.e., the equatorial
 164 center of the CS. In this case the size of the $+B_X$ hemisphere equals to that of the $-B_X$ hemisphere.
 165 Point P is an example of where a spacecraft could cross the CS. If the CS shifts toward either lobe
 166 (see the thin dashed blue lines), the lobe system becomes asymmetric and the crossing of the CS
 167 would occur at any of the points denoted as P' .

168 The angle, α , between the CS normal $\hat{\mathbf{n}}$ and the position vector \overrightarrow{OP} or $\overrightarrow{OP'}$ is $\approx 90^\circ$ if no
 169 significant shift occurs, and $\alpha > 90^\circ$ ($\alpha < 90^\circ$) if the CS is displaced toward the $+B_X$ hemisphere (-

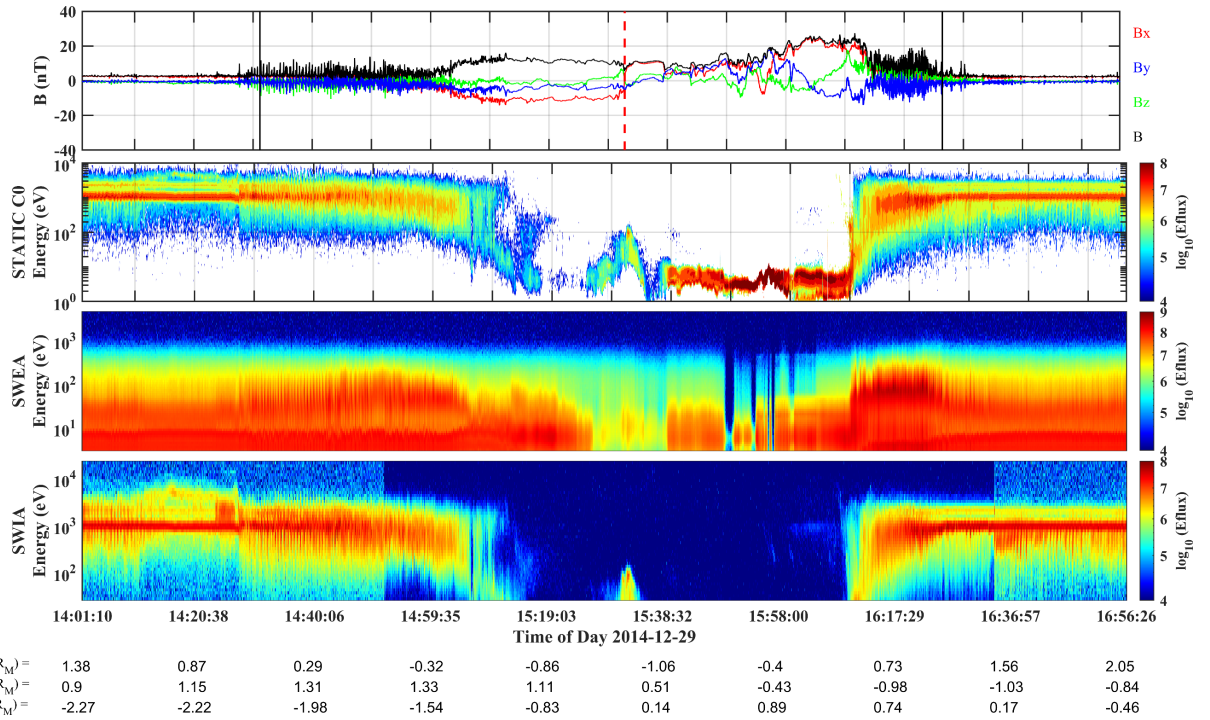
170 B_x hemisphere). The shifted distance can be estimated as $\Delta d = |\overline{OP'}| \cos \alpha$. The analysis on the
 171 shifted distance still holds on even $\hat{\mathbf{n}}$ has a significant n_x component. In this case, one just needs
 172 to replace $\hat{\mathbf{n}}$ by the cross-flow component $\hat{\mathbf{n}}_{\perp} = (0\mathbf{i}, n_y\mathbf{j}, n_z\mathbf{k})$.
 173 It should be noted that no IMF condition is applied using this technique: thus, the shifted distance
 174 can be calculated without knowing the simultaneous upstream IMF condition. Further, considering
 175 the angular uncertainty of CS normal via equation (2), the uncertainty of the shifted distance can
 176 be estimated as well.



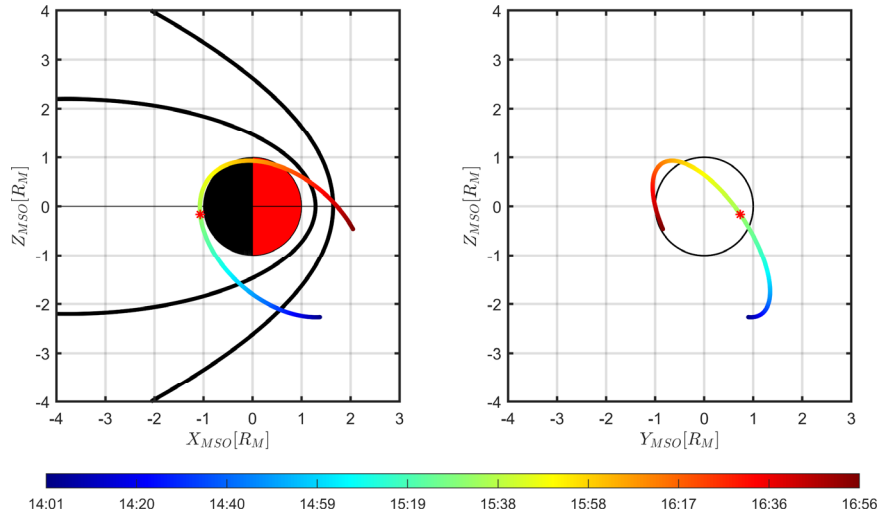
177
 178 **Figure 1.** The diagram illustrates the technique that evaluates the displacement of the CS. The
 179 thick blue line indicates the unshifted CS, and the CS crossing observed by MAVEN is at point P
 180 in this case. Similarly, the thin dashed blue lines represent a shifted CS, and the possible CS
 181 crossing points are the points P'. The CS normal at P or P' is represented by $\hat{\mathbf{n}}$ which points from
 182 $+B_x$ hemisphere to $-B_x$ hemisphere always. The angle, α , between $\overline{OP'}$ and $\hat{\mathbf{n}}$ is larger (less) than
 183 90° when CS is much displaced toward the $+B_x$ hemisphere ($-B_x$ hemisphere).

184 **4 Current Sheet Crossing Case Studies**

185 To systematically analyze the possible influence of the IMF flow-aligned component on the CS
 186 structure, we firstly will study three cases with a significant sunward flow component, a dominant
 187 cross-flow component and a dominant tailward flow component respectively for comparison.



188
 189 **Figure 2.** MAVEN crossing of the Martian magnetosphere on 29 December 2014. (the first to
 190 the fourth panel) The time series of magnetic field, the energy-time spectrogram of ions, electrons,
 191 and of solar wind ions. The position of MAVEN in MSO is given below the panels. The crossings
 192 of the bow shock and the tail CS are labeled by vertical black and red lines, respectively.



193

194 **Figure 3.** MAVEN trajectory in the XZ plane (left) and YZ (right) plane on 29 December 2014.
 195 In the XZ plane, the nominal bow shock (BS) and induced magnetosphere boundary (IMB) are
 196 marked by the black lines [Vignes et al., 2000]. The red star marks the CS crossing and the color
 197 bar indicates the time.

198 4.1 Case on 29 December 2014

199 As shown on Figure 2, MAVEN is crossing the Martian magnetosphere during 14:01-16:57 on
 200 29 December 2014. The time series plot of data from MAG, STATIC, SWEA and SWIA is shown
 201 in Figure, which displays the magnetic field and its three components in MSO coordinates and the
 202 energy-time spectrogram of electrons and ions.

203 As seen in Figure 2, the MAVEN crossings of the bow shock are indicated by the vertical black
 204 lines with a jump of the magnetic field and the distinct changes in the plasma spectrograms [Nagy
 205 et al., 2004]. The average IMF 30 min before the inbound bow shock crossing is seen as $\mathbf{B}_1 = [2.52,$
 206 $-0.90, -0.48]$ nT, while the average IMF after the outbound bow shock crossing yields $\mathbf{B}_2 = [2.34,$
 207 $-0.22, -0.84]$ nT, so the average IMF during the MAVEN magnetospheric crossing is $(\mathbf{B}_1 +$
 208 $\mathbf{B}_2)/2 = [2.43, -0.56, -0.66]$ nT, the cone angle (the angle between the +X direction and the IMF
 209 direction) of the IMF is 19° . Evidently, the IMF's orientation is significantly sunward, the IMF is
 210 dominated by the $+B_x$ component. Besides, the IMF remained comparatively steady before and
 211 after the bow shock crossings (seen the steady IMF definition in Section 4.4).

212 The current sheet crossing is marked by the red dashed vertical line at 15:32:44 UTC, when
 213 MAVEN is located at $[-1.07, 0.74, -0.16]$ R_M . The current sheet crossing is identified by the change

214 of the sign of B_x component, which changes from tailward to sunward. The current sheet crossing
 215 is also accompanied by the enhancement of the electron flux and ion flux [Halekas et al., 2006],
 216 which also indicate that MAVEN is indeed crossing the CS in the magnetotail.

217 Figure 3 illustrate MAVEN's trajectory from 14:01 UTC-16:56 UTC. Figure 3a provides a
 218 meridional plane view, while Figure 3b is the view from the tail toward the planet. The red stars
 219 present CS crossing. As described in Section 3, we performed the MVA method to the magnetic
 220 field data for the CS crossing and determined the CS normal direction. The MVA is applied to the
 221 magnetic field data at the CS crossing during 15:31:52-15:33:36, the maximum, intermediate and
 222 the minimum variance directions of the magnetic field are yielded as $\hat{\mathbf{L}} = [0.86, -0.51, 0.009]$, $\hat{\mathbf{M}} =$
 223 $[-0.17, -0.30, -0.94]$, $\hat{\mathbf{n}} = [0.48, 0.80, -0.35]$, respectively. In addition, the corresponding
 224 eigenvalues are $\lambda_1 = 51.2$, $\lambda_2 = 1.22$, $\lambda_3 = 0.31$ based on the calculations.

225 Applied the analysis technique introduced in section 3.2, the shift of the CS structure is
 226 quantitatively analyzed by calculating the angle, α , between the n_{\perp} and the position of the observed
 227 CS crossing position vector. The $\alpha \approx 11^\circ$ based on the calculation and the shift distance of the CS
 228 can be estimated as $\Delta d \sim 0.73R_M$, this indicates that the structure of CS is largely shifted towards
 229 the $-B_x$ hemisphere. In addition, as described in section 3.1 the accuracy of MVA results is
 230 inferred from the eigenvalues, the intermediate-to-minimum eigenvalue ratio here $\lambda_2/\lambda_3=3.9$,
 231 which indicates CS normal direction is well-determined. Apart from that, the distance of the
 232 crossing location to the equatorial plane is estimated as $R \sim 0.75R_M$. Thus, based on the angular
 233 uncertainty of $\hat{\mathbf{n}}$ relative to the orientation of $\hat{\mathbf{M}}$ via equation (3), the range of the shift distance of
 234 CS can be $\Delta d \in [0.72, 0.74] R_M$. The related parameters regarding the corresponding crossings are
 235 tabulated in Table 1.

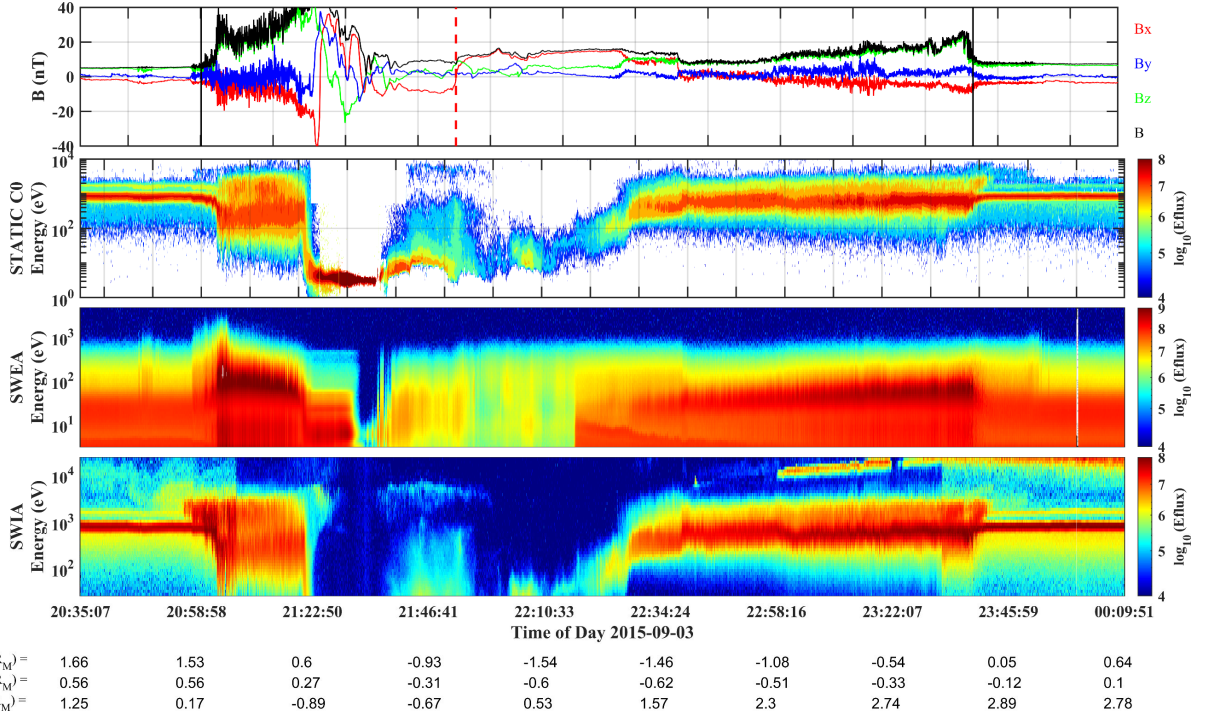
236 **Table 1:** The Parameters Related to the Current Sheet Crossing Cases.

Time	Location ^a (R_M)	IMF ^b	Cone Angle ^b	$\hat{\mathbf{n}}$	λ_2/λ_3	Δd^c
2014/12/29 15:32:44	(-1.07, 0.74, -0.16)	(2.43, -0.56, -0.66)	20°	(0.48 0.79 -0.35)	3.92	0.73 ∈ [0.72, 0.74]
2015/09/03 21:52:51	(-1.19, -0.42, -0.38)	(-3.10, 6.52, 0.19)	115°	(-0.11 0.73 -0.68)	10.81	-0.05 ∈ [-0.08, -0.02]
2018/02/19 00:47:08	(-0.68, -1.12, -0.20)	(-1.94, -0.63, 1.24)	145°	(0.12 0.18 0.98)	3.95	-0.40 ∈ [-0.50, -0.29]

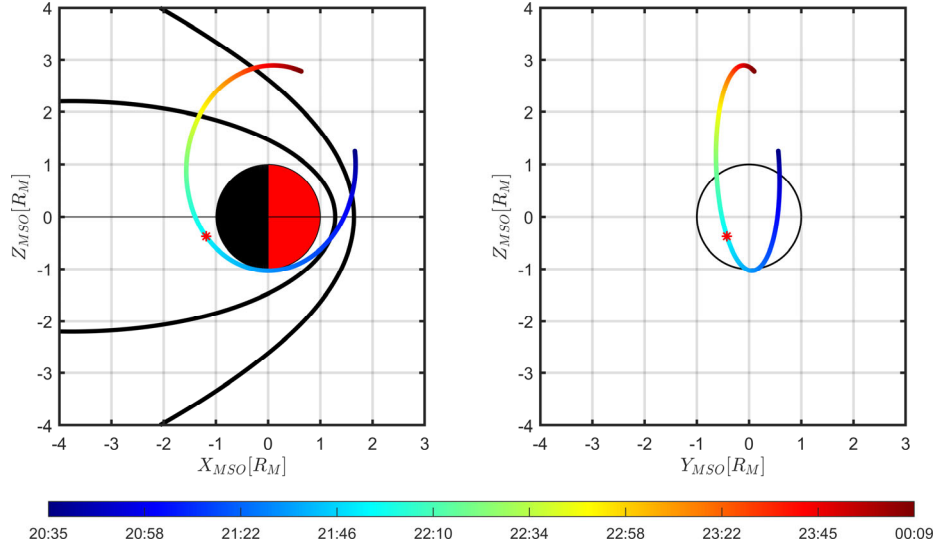
237 a: The location of current sheet crossing in MSO coordinates.

238 b: The averaged IMF and its cone angle.

239 c: The shifted distance of the current sheet plane. The sign “-” (+) represents the current sheet is shifted toward
 240 the $+B_X$ ($-B_X$) hemisphere, and vice versa. The range of the shifted distance is show in the square bracket.



241
 242 **Figure 4.** MAVEN crossing of the Martian magnetosphere on 3 September 2015. (the first to
 243 the fourth panel) The time series of magnetic field, the energy-time spectrogram of ions, electrons,
 244 and of solar wind ions. The crossings of the bow shock and the tail CS are labeled by vertical black
 245 and red lines, respectively.



246

 247 **Figure 5.** The MAVEN's trajectory on 3 September 2015. The format is the same with Figure 3.

248

4.2 Case on 3 September 2015

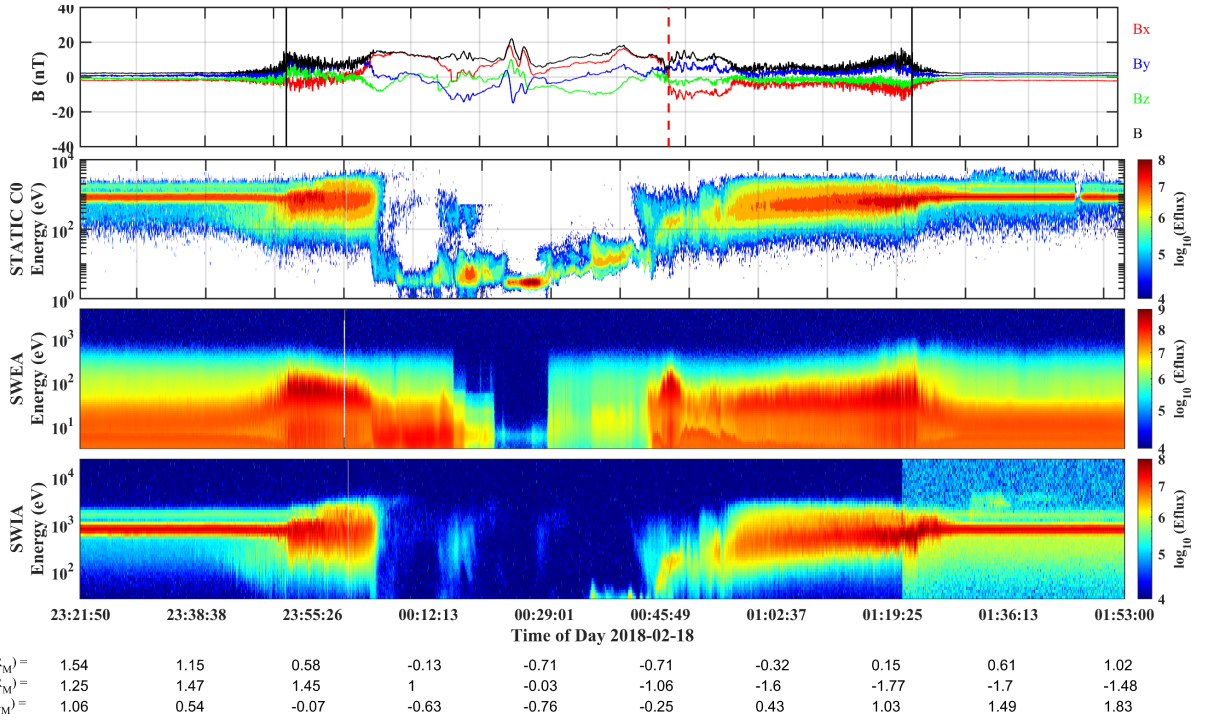
249

250 Another case is shown is Figure with a dominant cross-flow component, which occurred on 3
 251 September 2015. Similarly, the vertical black lines mark the inbound and outbound bow shock
 252 crossings at 21:05:07 and 23:39:51 respectively along with the fluctuations of the magnetic field
 253 and the ion energy spectrogram. The 30 min average before the inbound bow shock crossing yields,
 $\mathbf{B}_1 = [-2.84, 6.22, 0.27]$ nT, and $\mathbf{B}_2 = [-3.36, 6.83, 0.11]$ nT for the 30 min average after the outbound
 254 crossing, so the average IMF is $(\mathbf{B}_1 + \mathbf{B}_2)/2 = [-3.10, 6.52, 0.19]$ nT. The cone angle of the
 255 average IMF is $\sim 115^\circ$, which indicates that the IMF is dominated by cross-flow component during
 256 the entire Martian magnetosphere crossing while the B_x remained very steady.

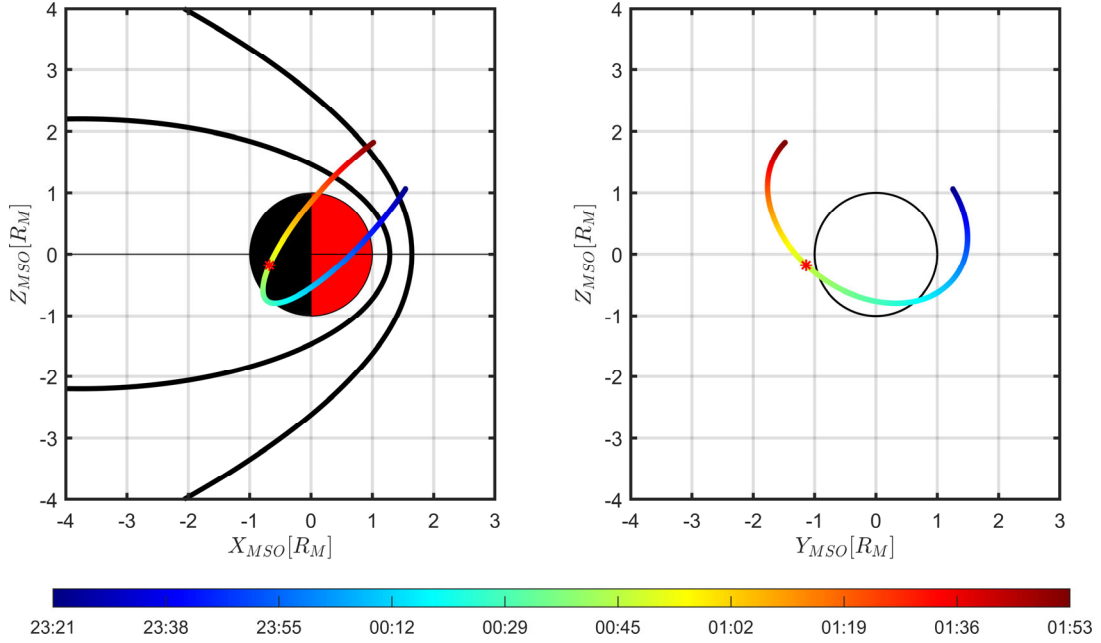
257

258 At 21:52:51 UTC, marked by the dashed red line, MAVEN is crossing the CS when located at
 259 $[-1.19, -0.42, -0.38]R_M$. The B_x component reverses from tailward to sunward as expected, along
 260 with the enhancement of ion flux and electron flux recorded by SWIA and SWEA instruments.
 261 Figure displays the trajectory of MAVEN in the XZ and YZ plane, the CS crossing is marked by
 262 red stars. As before, the MVA analysis is applied to the time interval 21:52:31- 21:53:11, the
 263 eigenvectors derived from the analysis are $\hat{\mathbf{L}} = [0.98, 0.22, 0.08]$, $\hat{\mathbf{M}} = [-0.21, 0.65, 0.73]$, $\hat{\mathbf{n}} = [-0.11,$
 264 $0.73, -0.68]$. The corresponding eigenvalues are $\lambda_1 = 11.4$, $\lambda_2 = 0.0893$, $\lambda_3 = 0.00826$,
 respectively.

265 With the same analysis technique before, it is estimated that the location of the CS crossing to
 266 the equatorial center of the CS plane is $R \sim 0.57 R_M$. The deviation angle α , between the CS normal
 267 vector and the position vector is about 95° , so we find that shifted distance of the CS is $\Delta d \sim -$
 268 $0.05 R_M$, which suggests that the CS does not shift significantly towards the $+B_x$ hemisphere
 269 under the cross-flow dominant IMF condition. Still, the uncertainty of the shifted distance can be
 270 estimated by equation (3), the range of the CS shifted distance can be derived as $\Delta d \in [-0.08, -$
 271 $0.02] R_M$.



272
 273 **Figure 6.** MAVEN crossing of the Martian magnetosphere on 18 and 19 February 2018. (the
 274 first to the fourth panel) The time series of magnetic field, the energy-time spectrogram of ions,
 275 electrons, and of solar wind ions. The crossings of the bow shock and the tail CS are labeled by
 276 vertical black and red lines, respectively.



277

278 **Figure 7.** The MAVEN's trajectory on 18 and 19 February 2018. The format is the same with
 279 Figure 3.

280

4.3 Case on 19 February 2018

281

282 As expected, Figure 6 shows a case with dominant tailward IMF B_x . In Figure 6, the vertical
 283 black lines represent the bow shock crossings at 23:51:50 and 01:23:00, respectively. The 30 min
 284 averaged IMF before the inbound bow shock crossing is $\mathbf{B}_1 = [-1.81, -0.92, 1.22]$ nT, while the
 285 averaged IMF after outbound crossing is $\mathbf{B}_2 = [-2.13, -0.33, 1.25]$ nT, the corresponding IMF is [
 286 1.97, -0.63, 1.24] nT and the cone angle is 145° . Clearly, the IMF is significantly tailward during
 the crossing of the Martian magnetosphere.

287

288 The CS crossing is marked by vertical red line at 00:47:08 when MAVEN is located at $[-0.68, -$
 289 $1.12, -0.2]R_M$, the sign of magnetic field B_x component changes along with the enhancement of
 290 energetic electron and ion flux. The MVA is applied over the interval 00:46:44- 00:47:32 during
 291 the magnetotail CS crossing event, the yielded eigenvectors are $\hat{\mathbf{L}} = [0.98, -0.19, -0.08]$, $\hat{\mathbf{M}} = [-0.17,$
 292 $-0.97, 0.20]$, $\hat{\mathbf{n}} = [0.12, 0.18, 0.98]$. The corresponding eigenvalues are $\lambda_1 = 11.8$, $\lambda_2 = 3.3$, $\lambda_3 =$
 293 0.84 , respectively. Then we calculated the deviation angle α between the $\hat{\mathbf{n}}_\perp$ and the position
 294 vector, which is 111° . The shifted distance can be estimated based on the angle as $\Delta d \sim -0.40 R_M$,
 which suggests the CS plane is largely displaced toward $+B_x$ hemisphere under the tailward

295 dominant IMF condition. Considering the angular uncertainty of $\hat{\mathbf{n}}$ relative to the orientation of $\hat{\mathbf{M}}$,
 296 the range of the CS shifted distance is estimated as $\Delta d \in [-0.50, -0.29]R_M$.

297 In summary, the analysis based on the selected three cases suggests that the IMF B_X seems to
 298 result in a systematic shift of the current sheet and a corresponding asymmetry of the structure.
 299 However, the selected cases cannot help us determine the possible correlations between the CS
 300 displacement and the IMF orientation. In that case, we enlarge the study with more cases based on
 301 the selection criteria described in the following subsection

302 **Table 2:** The table format is the same as Table 1 with more current sheet crossing cases.

Time	Location ^a (R_M)	IMF ^b	Cone Angle ^b	$\hat{\mathbf{n}}$	λ_2/λ_3	Δd^c
2014/12/29 15:32:44	(-1.07, 0.74, -0.16)	(2.43, -0.56, -0.66)	20°	(0.48 0.79 -0.35)	3.93	0.73 \in [0.72, 0.74]
2015/09/03 21:52:51	(-1.19, -0.42, -0.38)	(-3.10, 6.52, 0.19)	115°	(-0.11 0.73 -0.68)	10.81	-0.05 \in [-0.08, -0.02]
2018/02/19 00:47:08	(-0.68, -1.12, -0.20)	(-1.94, -0.63, 1.24)	145°	(0.12 0.18 0.98)	3.95	-0.40 \in [-0.50, -0.29]
2014/12/22 09:28:21	(-1.21, 0.55, -0.15)	(2.77, -3.24, -3.20)	59°	(-0.03 0.97 -0.24)	11.91	0.57 \in [0.56, 0.57]
2015/08/31 20:01:48	(-1.17, -0.49, -0.34)	(0.47, 4.43, -0.98)	84°	(0.22 -0.47 -0.85)	10.28	0.53 \in [0.52, 0.55]
2015/09/29 09:09:28	(-1.55, 0.14, -0.41)	(0.23, 2.19, -0.06)	84°	(-0.01 0.40 -0.92)	11.59	0.43 \in [0.430, 0.432]
2018/04/03 11:23:17	(-1.33, 0.15, -0.4)	(-0.19, -2.13, -0.06)	95°	(-0.23 -0.37 -0.90)	8.17	-0.43 \in [-0.43, -0.43]
2014/12/04 06:00:12	(-1.47, 0.05, -0.25)	(-0.58, 3.47, -1.56)	99°	(0.18 0.45 -0.88)	1.64	0.25 \in [0.23, 0.25]
2017/07/09 19:53:59	(-1.32, 1.08, -1.52)	(-3.10, 6.52, 0.19)	103°	(-0.29 -0.93 0.23)	4.47	-0.68 \in [-0.85, -0.43]
2014/12/05 09:40:14	(-1.30, -0.10, 0.13)	(-3.84, 2.98, -0.87)	141°	(0.23 0.97 -0.09)	5.33	-0.11 \in [-0.12, -0.10]
2016/02/02 11:02:04	(-1.00, -0.82, -0.31)	(-4.73, 0.61, 1.73)	159°	(0.33 0.85 0.42)	5.40	-0.87 \in [-0.88, -0.87]
2016/03/05 03:56:42	(-1.20, -0.12, 0.48)	(-1.34, -0.29, -0.59)	154°	(-0.73 0.1 -0.68)	9.31	-0.49 \in [-0.50, -0.49]
2018/03/14 12:41:51	(-1.17, -0.40, -0.39)	(-2.04, 1.41, 0.53)	144°	(0.17 0.91 -0.37)	10.71	-0.22 \in [-0.25, -0.20]
2016/08/15 20:30:25	(-1.10, -0.12, 0.37)	(3.28, 0.70, 1.31)	24°	(-0.35 -0.67 0.65)	15.52	0.34 \in [0.34, 0.35]

303 a: The location of current sheet crossing in MSO coordinates.

304 b: The averaged IMF and its cone angle.

305 c: The shifted distance of the current sheet plane. The sign “-” (+) represents the current sheet is shifted toward
306 the $+B_X$ ($-B_X$) hemisphere, and vice versa. The range of the shifted distance is show in the square bracket.

307

308 4.4 More cases

309 To systematically analyze whether the flow-aligned component can impact the CS structure and
310 cause the asymmetry in the Martian magnetotail, more CS crossing cases are selected for the
311 analysis. The magnetic field data of MAVEN with a 1-s time resolution from October 2014 to
312 February 2020 are adopted to select good current sheet crossing cases. The selection criteria are as
313 followed:

314 1. MAVEN should be located in the Martian magnetotail region, with region confinement
315 $-3R_M < X < -0.5R_M$, $\rho = \sqrt{Y^2 + Z^2} < 1.3R_M$.

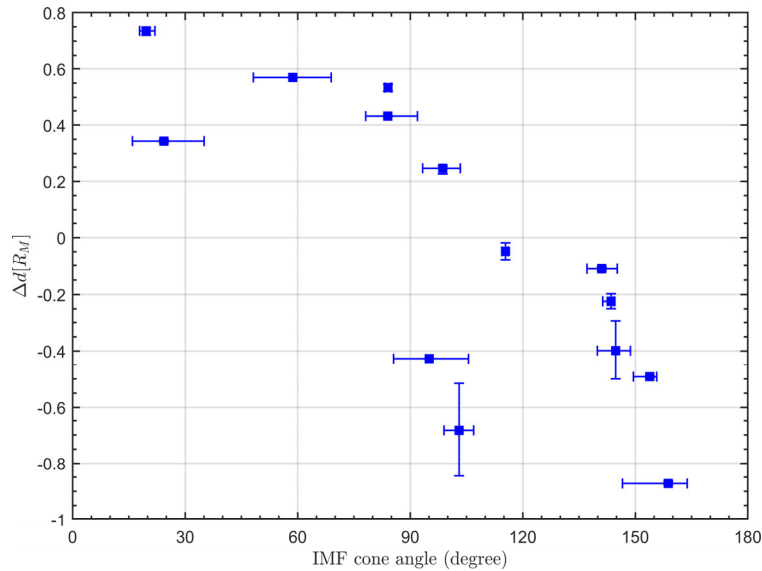
316 2. The CS crossings during the MAVEN magnetospheric crossings can be identified by the
317 change of B_X sign along with the enhancement of ions and electrons flux [*Halekas et al.*, 2006].
318 The CS should be assumed as stationary enough during the crossing, so evident flapping event
319 of the CS should not occur during the crossing [*Rong et al.*, 2015a, 2015b; *DiBraccio et al.*,
320 2017] and the CS crossing should only occur one time during the magnetotail crossing. In that
321 case, further analysis of the CS structure shift can be made.

322 3. To get steady IMF crossings, the upstream IMF component should fulfill the steady criteria
323 [*Rong et al.*, 2014, 2016]: the 30 min averaged IMF before the inbound bow shock crossing
324 are denoted as \mathbf{B}_1 , while \mathbf{B}_2 represents the 30 min averaged IMF after the outbound bow shock
325 crossing (A list of MAVEN bow shock crossings from October 2014 to February 2020 can be
326 found in the supporting information). The criteria regarding angle and strength should be
327 fulfilled to meet the steady requirement: the deviation angle α between \mathbf{B}_1 and \mathbf{B}_2 should be
328 less than 30° and the perturbations of IMF strength should satisfy $\frac{2\|\mathbf{B}_1\| - \|\mathbf{B}_2\|}{\|\mathbf{B}_1\| + \|\mathbf{B}_2\|} < 0.2$. Then the
329 averaged upstream IMF of the MAVEN crossing is $(\mathbf{B}_1 + \mathbf{B}_2)/2$.

330 4. To make a better analysis, no large fluctuations should occur in the upstream IMF: we visually
331 picked out the good CS crossing cases from all the magnetospheric crossings which the IMF
332 30 min before the bow shock inbound crossing and after the outbound crossing show no evident
333 fluctuations.

334 5. To avoid the potential influence of the crustal magnetic fields, the CS crossing should be above
 335 at least 400 km when MAVEN is flying above the strong crustal magnetic field regions.

336 More cases (total 14 cases) were selected for studies based on the above criteria, the related
 337 parameters regarding the CS crossing are tabulated in Table 2. Based on the analysis of these cases,
 338 Figure 8 shows the shifted distance Δd of CS as a function of the upstream IMF cone angle. A
 339 correlation can be seen between the shifted distance and the IMF cone angle, the shifted distance
 340 varies inversely with the IMF cone angle, that is the shifted distance $|\Delta d| \gg 0$ when the IMF cone
 341 angle is much less or more than 90° , and vice versa. However, the inverse correlation is not evident
 342 for two of the selected cases. The ratio λ_2/λ_3 of case one with cone angle 99° is 1.6, so the reason
 343 accounted for this inconsistency may be the less well-determined current sheet normal direction
 344 estimated by the MVA. The inconsistency of the other cases may be caused by other unknown
 345 reasons, since some other factors may also displace the current sheet structure to some degree.
 346 From the results of the carefully selected CS crossing cases, there seems to be a correlation
 347 between the displacement of the CS structure and the IMF cone angle. The CS appears to be shifted
 348 more to the +Y direction, when the IMF cone angle is much less than 90° , while the CS appears
 349 shifted to the -Y direction, when the IMF cone angle is much greater than 90° .



350

351 **Figure 8.** Scatter plot represents the shifted distance of the CS as a function of the IMF cone angle.
 352 The lengths of the horizontal error bars represent the IMF cone angle deviation between the IMF

353 for inbound and outbound bow shock crossings. The lengths of the vertical error bars represent
 354 the uncertainty of the shifted distance from the uncertainty of the CS normal estimated by the MVA.

355 **5 Statistical Analysis**

356 Analysis based on selected CS crossing cases suggest the possible inverse correlation between
 357 the shifted distance of the CS and the cone angle of upstream IMF. However, one may argue that
 358 the biased selection of the CS crossing cases would make the results unreliable. As a result, it is
 359 of great importance to statistically check the effects of the IMF flow-aligned component (B_X) on
 360 the average configurations of the CS structures in magnetotail. To statistically study the influences
 361 of the IMF, the magnetic field data of MAVEN MAG from October 2014 to February 2020 are
 362 adopted to the analysis.

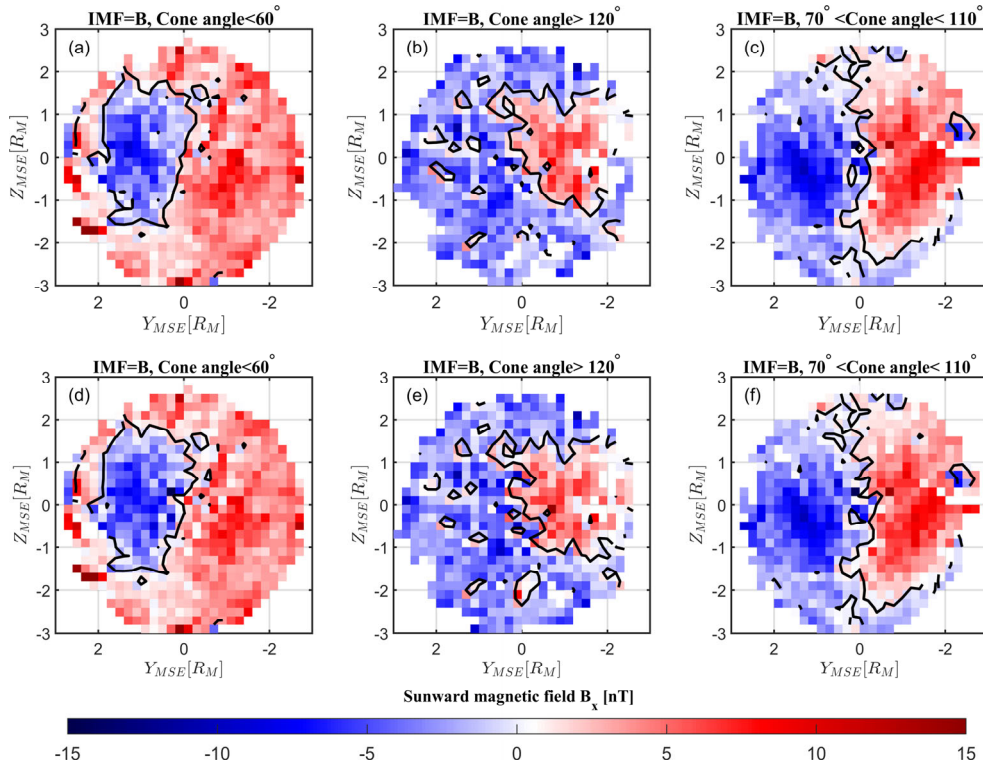
363 The statistical analysis is made in Mars-Solar-Electric field (MSE) coordinate system. This
 364 involves a transformation in the Y-Z plane by calculating the direction of the solar wind convection
 365 electric field (\mathbf{E}_{SW}) on the basis of the anti-sunward solar wind flow (\mathbf{V}_{sw}) in the $-X_{MSO}$ direction
 366 and IMF orientation ($\mathbf{B}_{IMF_{YZ}}$) perpendicular to the solar wind flow: $\mathbf{E}_{SW} = -\mathbf{V}_{sw} \times \mathbf{B}_{IMF_{YZ}}$.
 367 \mathbf{E}_{SW} is positive along the Z_{MSE} direction, and therefore $-\mathbf{V}_{sw}$ and $\mathbf{B}_{IMF_{YZ}}$ oriented in the
 368 direction of X_{MSE} and Y_{MSE} , respectively. In MSE coordinates, the Z_{MSE} axis is basically
 369 contained in the CS plane which is nominally located at $Y_{MSE} \sim 0$.

370 Similar as the previous analysis, the procedures implemented in previous studies [Rong *et al.*,
 371 2014, 2016] are adopted which is, we select orbits when the upstream IMF satisfy the steady
 372 requirements defined in section 4.4 (there are total 1445 magnetospheric crossings fulfilling the
 373 criteria), and then the MAVEN magnetic field data are transformed into MSE coordinates with
 374 region confinement ($-3R_M < X_{MSE} < -0.5R_M$). Here the MSE coordinate system is computed
 375 using the averaged upstream IMF ($\mathbf{B} = (\mathbf{B}_1 + \mathbf{B}_2)/2$) and the corresponding solar wind velocity
 376 measured by SWIA.

377 To find the average configurations of the CS structure, we look at the B_X component spatial
 378 distributions in the MSE Y-Z plane and the size of the spatial bins are $0.2 \times 0.2R_M$. We further
 379 compute the contours of $B_X=0$ in the plane. The contours of $B_X=0$ near $Y_{MSE} \sim 0$ can be seen as the
 380 average configuration of the CS structure. To analyze the IMF flow-aligned component effects on
 381 the CS configurations, the investigations are carried out under different IMF conditions, the

382 significant sunward IMF (cone angle $<60^\circ$, 500 magnetospheric crossings) and tailward IMF (cone
 383 angle $>120^\circ$, 260 magnetospheric crossings), along with the cross-flow IMF ($70^\circ <$ cone
 384 angle $<110^\circ$, 439 magnetospheric crossings). Figure 9 shows the spatial distributions of the IMF
 385 B_X in the MSE coordinates, Figure 9 (a)-(c) corresponds the sunward, tailward and cross-flow IMF
 386 condition respectively. In addition, the contours of $B_X=0$ are generated automatically by the
 387 MATLAB with an interpolation technique of its own, therefore the contour will pass through some
 388 spatial bins where $B_X \neq 0$ unavoidably. It should be noted that some ‘‘circle structure’’ of the
 389 contours appear in the lobe, there are no particular meanings for these circles, they are likely to be
 390 produced by the IMF uncertainty in some cases.

391

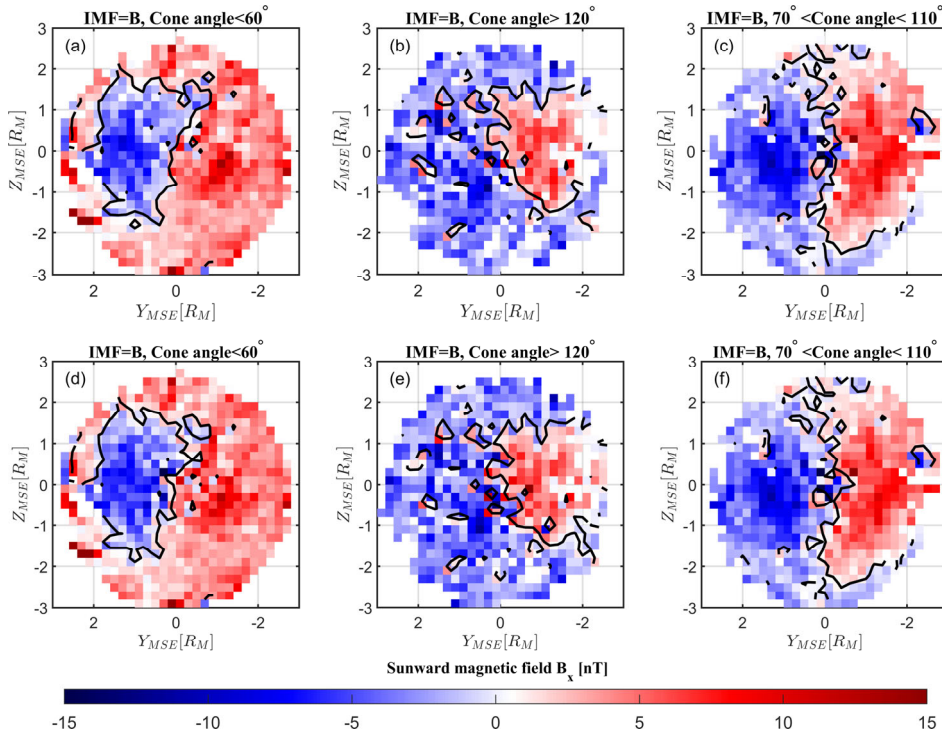


392

393 **Figure 9.** The distribution of the B_X component in the modified Mars-Solar-Electric field (MSE)
 394 coordinates ($-3 R_M < X_{MSE} < -0.5 R_M$) when the average upstream IMF ($\mathbf{B} = (\mathbf{B1} + \mathbf{B2})/2$) is
 395 significantly (a) sunward (cone angle $<60^\circ$) and (b) tailward (cone angle $>120^\circ$) (c) cross-flow
 396 ($70^\circ <$ cone angle $<110^\circ$). The average configurations of the tail current sheet structure are
 397 marked by the solid black lines. (a)-(c) represent the current sheet configurations without crustal

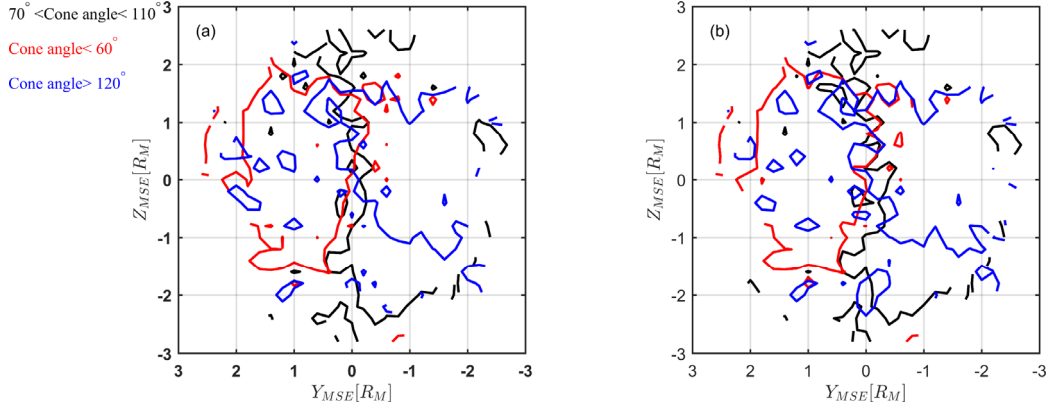
398 magnetic fields effects. (d)-(f) represent the current sheet configurations with crustal magnetic
 399 fields effects.

400 To also look at the influence of the crustal fields, the average CS configurations are compared
 401 as well when the crustal fields are included and omitted conditions in this statistical study. To filter
 402 out the influence of the strongest crustal magnetic fields, we discarded magnetic field data recorded
 403 by MAVEN when it is flying above the strongest crustal fields region ($130^\circ - 230^\circ$ in longitude
 404 of the southern hemisphere) in the magnetotail region. Figure 9 (d)-(f) corresponds the sunward,
 405 tailward and cross-flow IMF condition with strong crustal magnetic fields considered. Considering
 406 the limited coverage of the crustal magnetic field effects, we also compared the crustal field effects
 407 at the near Mars magnetotail using the different region confinement ($-1.5R_M < X_{MSE} < -0.5R_M$)
 408 as shown in Figure 10.



409
 410 **Figure 10.** The distribution of the B_x component in the modified Mars-Solar-Electric field
 411 (MSE) coordinates ($-1.5 R_M < X_{MSE} < -0.5 R_M$) when the average upstream IMF ($\mathbf{B} =$
 412 $(\mathbf{B1} + \mathbf{B2})/2$) is significantly (a) sunward (cone angle $< 60^\circ$) and (b) tailward (cone angle $> 120^\circ$)
 413 (c) cross-flow ($70^\circ < \text{cone angle} < 110^\circ$). The average configurations of the tail current sheet
 414 structure are marked by the solid black lines. (a)-(c) represent the current sheet configurations

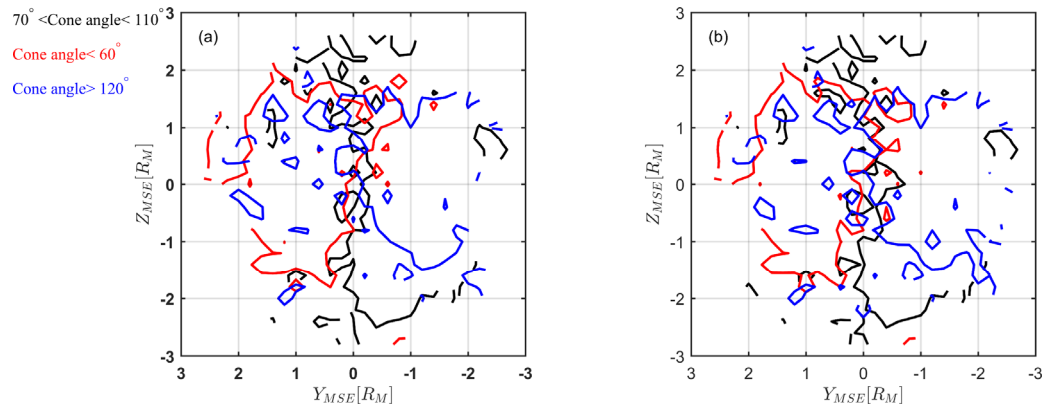
415 without crustal magnetic fields effects. (d)-(f) represent the current sheet configurations with
 416 crustal magnetic fields effects.



417

418 **Figure 11.** The average configuration of the magnetotail current sheet (the contour of $B_X = 0$
 419 near $Y_{MSE} \sim 0$) when IMF is significantly sunward (red lines), tailward (blue lines) and cross-
 420 flow (black line).

421



422

423 **Figure 12.** The format is the same as Figure 11, with region confinement ($-1.5 R_M < X_{MSE} <$
 424 $-0.5 R_M$).

425

426 The structure of the CS, however, is not always aligned with the solar wind motional electric
 427 field (E_{SW}) as one would expect, the average configurations of the CS are actually sensitive to the
 428 value of the IMF cone angle as shown in Figure 8, which suggests that the displacement of the CS
 429 structure is influenced by the flow-aligned component of the IMF. In addition, the offset of the CS

430 structure in the MSE coordinates is systematically controlled by the IMF orientation as presented
 431 in Figure 9 and Figure 10, the CS is shifted to the dusk (+Y) when the IMF is significantly
 432 sunward $+B_x$ hemisphere, and shifted to the dawn (-Y) when the tailward IMF is dominant and
 433 resulting in a dominant $-B_x$ hemisphere of the magnetic lobes, while the CS is nearly located at
 434 $Y_{MSE} \sim 0$ during the cross-flow dominant IMF conditions, and the situations are nearly identical for
 435 the observations made in the near Mars magnetotail region ($-1.5 R_M < X_{MSE} < -0.5 R_M$).
 436 Considering the effects from the crustal fields, the general configurations of the CS are similar
 437 when the crustal fields are included, there are indeed some minor changes in the CS structures near
 438 $Z_{MSE} \sim 0$ where the strong crustal magnetic fields are present. As for the near Mars magnetotail,
 439 the average configurations of the CS tend to be much more variant, part of the curves are offset
 440 when the crustal fields are included, the comparison between the included and excluded crustal
 441 fields observations further confirm the effects of crustal fields on current sheet configurations in
 442 Martian magnetotail. [Halekas *et al.*, 2006; Luhmann *et al.*, 2015]. But from our statistical studies,
 443 we can tell that the shift of the current sheet structure is dominated by the flow-aligned component
 444 of IMF systematically, with some minor contributions from the crustal magnetic fields.

445 Moreover, Liemohn *et al.* [2017] found the asymmetry of the current sheet may also be
 446 controlled by ionospheric conditions, the current sheet is shifted to the dawn (-Y) during solar
 447 maximum and to the dusk (+Y) during solar minimum. Their MHD simulation results suggest the
 448 shift is not a function of crustal fields or solar wind conditions, since they are omitted and held
 449 constant in their study. Based on their study, we also roughly considered the effects of solar EUV
 450 intensity, due to the limited operation time length of MAVEN, we choose the perihelion (1.38-
 451 1.52 AU) and aphelion (1.52-1.66 AU) to compare the solar EUV intensity effects. The
 452 configurations of the CS are slightly different in when considering the solar EUV intensity effects,
 453 but as still the IMF flow-aligned component is the dominant factor for current sheet configuration
 454 shift (Figures presented in supplementary files). We cannot conclude whether the configuration
 455 differences are caused by solar EUV intensity or the change of IMF conditions, so further
 456 quantitative studies on the solar EUV intensity effects on current sheet structure shift based on
 457 MAVEN observations may be required in the future to confirm that.

458 Based on above results, the statistical studies we carried out above support our conclusions from
 459 the selected individual cases: the shift of the current sheet structure in Martian magnetotail is

460 dominantly controlled by the flow-aligned component of IMF (B_X), with contributions from other
461 factors like the crustal magnetic fields.

462 **6 Discussion and Conclusions**

463 In this work, based on carefully selected cases as well as a statistical study using MAVEN
464 magnetic field data from October 2014 to February 2020. We found an appreciable dependence
465 between the shift of the current sheet structure and the flow-aligned component of the IMF as
466 shown in Figure 8. The Mars magnetotail current sheet is located shifted toward the $-B_X$
467 hemisphere for the significant sunward IMF cases and then moves to the $+B_X$ hemisphere for the
468 tailward IMF cases, while cross-flow dominant IMF cannot significantly displace the current sheet
469 structure in the Martian magnetotail. Besides, by comparing the average configurations of
470 magnetotail current sheet structure in the modified MSE coordinates shown in Figure 9 and Figure
471 10. We can tell that IMF flow-aligned component (IMF B_X) is able to significantly impact the
472 current sheet structure of the near-Mars magnetotail. Moreover, with crustal magnetic fields
473 discarded data set and the normal data set comparison, it is showed that the current sheet structure
474 can indeed be influenced by the crustal magnetic fields, as previous studies suggested [*Ma et al.*,
475 2002; *Harnett and Winglee*, 2005; *Fang et al.*, 2010, 2015; *Dong et al.*, 2015]. Moreover, from the
476 comparison we can tell that the dominant controlling factor for the magnetotail current sheet
477 structure is the IMF orientation with some contributions from other factors like the crustal
478 magnetic fields and solar EUV intensity [*Liemohn et al.*, 2017], even though the effects from the
479 crustal magnetic fields may be averaged to some degree.

480 Our study demonstrates that the significant CS displacement (shown in Figure 8) and the lobe
481 asymmetry of the CS structure (shown in Figure 9 and Figure 10) does show a correlation with the
482 dominant IMF B_X . However, some further discussions will be needed to present possible
483 explanations accounting for the inconsistency between previous results and our study, to point out
484 the differences between the space environment of Venus and Mars. With the similar analysis
485 technique, the study by *Rong et al.* [2016] found no evident correlations between the IMF
486 orientation and asymmetries of the magnetic field structure in the near-Venus magnetotail. Their
487 results are inconsistent with the study by *McComas et al.* [1986], they gave two possible
488 explanations for the inconsistency (see their discussion and conclusion): 1. The asymmetry may
489 be caused by other unknown reasons (e.g., the biased data set of PVO, since PVO spent little time

490 measuring the upstream solar wind and IMF) 2. The IMF B_x can impact the magnetic field
491 structure, but is not significant in the near-Venus magnetotail where their observations were made.
492 However, in our study the systematic asymmetry of the current sheet structure controlled by the
493 IMF can be observed by MAVEN in the near-Mars magnetotail. Here we attempt to present some
494 simple physical interpretations and discuss the possible reasons for the difference from the
495 perspective of both the numerical simulations and theoretical analysis.

496 A previous study by *Romanelli et al.* [2014] presented the theoretical analysis between the
497 interaction of the solar wind and the unmagnetized planets. They analytically addressed an ideal
498 non-collisional interaction between conducting obstacles and magnetized plasma winds, where a
499 perfectly magnetized magnetohydrodynamic (MHD) plasma (no resistivity) under steady state
500 conditions flows around a spherical body for various orientations of the streaming magnetic field.
501 The arbitrary orientation of the magnetic field was seen as the combination of a linear combination
502 of the flow-aligned component and the cross-flow component in their study. Most of the structures
503 and characters of the induced magnetosphere (e.g. the classical draping configuration) can be
504 reproduced by their approach. Moreover, they found that when the external magnetic field is
505 strictly perpendicular to the direction of the flow, the induced magnetotail formed downstream
506 from the obstacle consists of two mirror-symmetric magnetic hemispheres separated by a flat PRL
507 (polarity reverse layer, actually the magnetotail current sheet), the PRL is always in the same plane
508 regardless of the orientation of the background magnetic field. In other words, the PRL cannot be
509 displaced by the flow-aligned component of the magnetic field, which is consistent with the
510 observations by *Rong et al.* [2016]. In addition, the IRPL (inverse polarity reverse layer, the
511 boundary layer of magnetotail) appears when there is a significant flow-aligned component in the
512 magnetic field, and the IRPL also appears in IMF B_x dominant case 1 and case 2 in the Venus
513 magnetotail of *Rong et al.* [2016] (see Figure 5). It should be noted that *Romanelli et al.* [2014]
514 only addressed the ideal MHD case without any resistivity. However, another work by *Romanelli*
515 *et al.* [2015] (see their introduction) suggested that the inclusion of resistivity must result in a shift
516 of the tail current sheet as reported by *McComas et al.* [1986].

517 Apart from theoretical analysis, results from simulations (e.g. hybrid simulations and MHD
518 simulations) can also help us interpret the possible reasons for the different magnetotail
519 configurations. As mentioned in Introduction, the nonideal MHD simulation of the Venus space
520 environment (with particle collisions and resistivity) by *Ma et al.* [2013] showed the flow-aligned

521 component of the IMF influences the magnetic field configuration of the Venusian magnetotail
522 systematically, which is consistent with our observations. In addition, the hybrid simulation of
523 Titan by *Simon et al.* [2009] also showed that the dominant flow-aligned magnetic field component
524 goes along with the corresponding asymmetry of Titan's magnetotail. Therefore, the nonideal
525 MHD simulations as well as the hybrid simulations show good agreement with our observations,
526 suggesting the possibility that particle collisions and effects of resistivity favor a displacement of
527 the magnetotail current sheet under dominant IMF B_x conditions. Moreover, the simulation results
528 mentioned above do not align with *Romanelli et al.* [2014] and *Rong et al.* [2016]. Based on that,
529 we may infer the difference between the space environment of Mars and Venus, which is the
530 resistivity effects may not be significant for near-Venus magnetotail formation compared with
531 near-Mars magnetotail. In that case, we need to further discuss the results from ideal MHD
532 simulations.

533 The results from ideal MHD simulations [*Zhang et al.*, 2009] showed that the induced
534 magnetosphere of Venus totally disappear under the extreme flow-aligned IMF orientation. The
535 field lines are excluded from the Venus wake. The simulation results are understandable, since the
536 flow-aligned magnetic field upstream must indicate a flow-aligned downstream according to MHD
537 Rankie-Hugoniot conditions. If the IMF can simply be seen as the linear combination of the flow-
538 aligned and cross-flow component as is the case in the ideal problem addressed by *Romanelli et*
539 *al.* [2014], the results of *Rong et al.* [2016] are easy to be interpreted. Any IMF orientation can be
540 decomposed into a cross-flow component and a flow-aligned component (IMF B_x). In terms of
541 ideal MHD, the flow-aligned component cannot penetrate into magnetotail, only cross-flow can
542 contribute to the formation of the magnetotail. Thus, the results of *Rong et al.* [2016] suggested
543 that the flow-aligned dominant IMF cannot significantly influence the magnetotail, since the solar
544 wind can be seen as the steady state in their statistical studies based on their selection criteria,
545 which perfectly satisfied the assumption of *Romanelli et al.* [2014], so their observations of the
546 near-Venus magnetotail can be well described by the ideal MHD situation.

547 Based on above discussion, we may infer the possible reason for the inconsistency between our
548 observations and the previous study [*Rong et al.*, 2016, Figure 11]. From the perspective of
549 theoretical analysis and numerical simulations, the different significance of particle effects and
550 resistivity on Mars and Venus may play a role in the magnetotail shift. For Venus, neither the
551 hybrid nor the MHD simulation are consistent with the observation by *Rong et al.* [2016], so it

552 may imply that either the related particle effects, e.g., particle collisions and wave particle
553 interaction, cannot significantly impact the magnetic field structure of the Venusian magnetotail.
554 Some unknown effects other than the IMF B_x component that gives the shift and asymmetric
555 structure of CS may balance the particle effects to make the CS unshifted significantly. For Mars,
556 due to the smaller ion gyroradii and effects from crustal magnetic fields, particle effects may play
557 a more important role in the near-Mars magnetotail. In that case, particle collisions and effects of
558 resistivity may indeed favor a displacement of the magnetotail current sheet under dominant IMF
559 B_x conditions. In all, the inconsistency between the observations of near-Mars and near-Venus
560 magnetotail are possibly related to different particle effects of the planetary space environment,
561 based on results from numerical simulations, theoretical analysis along with satellite observations.

562 In conclusion, the comparison of theoretical analysis and numerical simulations show that when
563 the particle effects in the form of resistivity are included, the magnetotail current sheet would be
564 systematically controlled by the IMF orientation as shown in our observations of the near-Mars
565 magnetotail. While in *Rong et al.* [2016], the statistical study suggested the effects of resistivity
566 appearing in the models do not play a significant role in the formation of the near-Venus
567 magnetotail. The different results between Mars and Venus may imply the different role of particle
568 effects in the magnetotail of the two planets, further simulation and observation will be needed to
569 confirm the effects. Moreover, the displacement of the current sheet following the orientation of
570 the IMF has also consequences on the location of the region where planetary particle acceleration
571 is expected. Therefore, the displacement of the current sheet structure should be taken into account
572 when estimating the planetary ion escape rate in the magnetotail. In all, future comparative and
573 more comprehensive studies on Venus, Mars, and Titan may help us discover more about the
574 factors that may displace the structure of the induced magnetotail and improve our knowledge
575 about the space environment of these unmagnetized planets.

576 **Acknowledgments**

577 The MAVEN data used for this study are publicly available from the NASA Planetary Data System
578 (<https://pds-ppi.igpp.ucla.edu/>). Y. Z. Wen is supported by undergraduate research fellowship
579 from Chinese Academy of Sciences. Z. J. Rong is funded by National Natural Science Foundation
580 of China (Grant). The authors would like to thank the MAVEN team for the data and mission
581 support.

582

583 **References**

- 584 1. Bertucci C, Duru F, Edberg N, Fraenz M, Martinecz C, Szego K, Vaisberg O. (2011). The
 585 Induced Magnetospheres of Mars, Venus, and Titan. *SPACE SCI REV*, 162(1-4), 113-171. doi:
 586 10.1007/s11214-011-9845-1
- 587 2. Connerney JEP, Espley J, Lawton P, Murphy S, Odom J, Oliverson R, Sheppard D. (2015). The
 588 MAVEN Magnetic Field Investigation. *SPACE SCI REV*, 195(1-4), 257-291. doi:
 589 10.1007/s11214-015-0169-4
- 590 3. DiBraccio GA, Dann J, Espley JR, Gruesbeck JR, Soobiah Y, Connerney JEP, Halekas JS,
 591 Harada Y, Bowers CF, Brain DA, Ruhunusiri S, Hara T, Jakosky BM. (2017). MAVEN
 592 observations of tail current sheet flapping at Mars. *Journal of Geophysical Research: Space*
 593 *Physics*, 122(4), 4308-4324. doi: 10.1002/2016JA023488
- 594 4. DiBraccio GA, Espley JR, Gruesbeck JR, Connerney JEP, Brain DA, Halekas JS, Mitchell DL,
 595 McFadden JP, Harada Y, Livi R, Collinson G, Hara T, Mazelle C, Jakosky BM. (2015).
 596 Magnetotail dynamics at Mars: Initial MAVEN observations. *GEOPHYS RES LETT*, 42(21),
 597 8828-8837. doi: <https://doi.org/10.1002/2015GL065248>
- 598 5. Dong C, Bougher SW, Ma Y, Toth G, Lee Y, Nagy AF, Tennishev V, Pawlowski DJ, Combi
 599 MR, Najib D. (2015). Solar wind interaction with the Martian upper atmosphere: Crustal field
 600 orientation, solar cycle, and seasonal variations. *Journal of Geophysical Research: Space*
 601 *Physics*, 120(9), 7857-7872. doi: <https://doi.org/10.1002/2015JA020990>
- 602 6. Dubinin E, Fraenz M. (2015). Magnetotails of Mars and Venus. *Magnetotails in the solar*
 603 *system*, 207, 34-59
- 604 7. Fang X, Liemohn MW, Nagy AF, Luhmann JG, Ma Y. (2010). On the effect of the martian
 605 crustal magnetic field on atmospheric erosion. *ICARUS*, 206(1), 130-138. doi:
 606 <https://doi.org/10.1016/j.icarus.2009.01.012>
- 607 8. Fang X, Liemohn MW, Nagy AF, Ma Y, De Zeeuw DL, Kozyra JU, Zurbuchen TH. (2008).
 608 Pickup oxygen ion velocity space and spatial distribution around Mars. *Journal of Geophysical*
 609 *Research: Space Physics*, 113(A2). doi: <https://doi.org/10.1029/2007JA012736>
- 610 9. Halekas JS, Brain DA, Lillis RJ, Fillingim MO, Mitchell DL, Lin RP. (2006). Current sheets at
 611 low altitudes in the Martian magnetotail. *GEOPHYS RES LETT*, 33(13). doi:
 612 10.1029/2006GL026229

- 613 10. Halekas JS, Taylor ER, Dalton G, Johnson G, Curtis DW, McFadden JP, Mitchell DL, Lin RP,
614 Jakosky BM. (2015). The Solar Wind Ion Analyzer for MAVEN. *SPACE SCI REV*, 195(1-4),
615 125-151. doi: 10.1007/s11214-013-0029-z
- 616 11. Harnett EM. (2005). Three-dimensional fluid simulations of plasma asymmetries in the
617 Martian magnetotail caused by the magnetic anomalies. *Journal of Geophysical Research*,
618 110(A7). doi: 10.1029/2003JA010315
- 619 12. Jakosky BM, Lin RP, Grebowsky JM, Luhmann JG, Mitchell DF, Beutelschies G, Priser T,
620 Acuna M, Andersson L, Baird D, Baker D, Bartlett R, Benna M, Bougher S, Brain D, Carson
621 D, Cauffman S, Chamberlin P, Chaufray JY, Cheatom O, Clarke J, Connerney J, Cravens T,
622 Curtis D, Delory G, Demcak S, DeWolfe A, Eparvier F, Ergun R, Eriksson A, Espley J, Fang
623 X, Folta D, Fox J, Gomez-Rosa C, Habenicht S, Halekas J, Holsclaw G, Houghton M, Howard
624 R, Jarosz M, Jedrich N, Johnson M, Kasprzak W, Kelley M, King T, Lankton M, Larson D,
625 Leblanc F, Lefevre F, Lillis R, Mahaffy P, Mazelle C, McClintock W, McFadden J, Mitchell
626 DL, Montmessin F, Morrissey J, Peterson W, Possel W, Sauvaud JA, Schneider N, Sidney W,
627 Sparacino S, Stewart AIF, Tolson R, Toubanc D, Waters C, Woods T, Yelle R, Zurek R.
628 (2015). The Mars Atmosphere and Volatile Evolution (MAVEN) Mission. *SPACE SCI REV*,
629 195(1-4), 3-48. doi: 10.1007/s11214-015-0139-x
- 630 13. Liemohn MW, Xu S, Dong C, Bougher SW, Johnson BC, Ilie R, De Zeeuw DL. (2017).
631 Ionospheric control of the dawn - dusk asymmetry of the Mars magnetotail current sheet.
632 *Journal of Geophysical Research: Space Physics*, 122(6), 6397-6414. doi:
633 10.1002/2016JA023707
- 634 14. Luhmann JG, Dong C, Ma Y, Curry SM, Mitchell D, Espley J, Connerney J, Halekas J, Brain
635 DA, Jakosky BM, Mazelle C. (2015). Implications of MAVEN Mars near-wake measurements
636 and models. *GEOPHYS RES LETT*, 42(21), 9087-9094. doi:
637 <https://doi.org/10.1002/2015GL066122>
- 638 15. Ma Y. (2002). Three-dimensional multispecies MHD studies of the solar wind interaction with
639 Mars in the presence of crustal fields. *Journal of Geophysical Research*, 107(A10). doi:
640 10.1029/2002JA009293
- 641 16. Ma YJ, Nagy AF, Russell CT, Strangeway RJ, Wei HY, Toth G. (2013). A global multispecies
642 single-fluid MHD study of the plasma interaction around Venus. *Journal of Geophysical
643 Research: Space Physics*, 118(1), 321-330. doi: 10.1029/2012JA018265

- 644 17. McComas DJ, Spence HE, Russell CT, Saunders MA. (1986). The average magnetic field
645 draping and consistent plasma properties of the Venus magnetotail. *Journal of Geophysical*
646 *Research*, 91(A7), 7939. doi: 10.1029/JA091iA07p07939
- 647 18. McFadden JP, Kortmann O, Curtis D, Dalton G, Johnson G, Abiad R, Sterling R, Hatch K,
648 Berg P, Tiu C, Gordon D, Heavner S, Robinson M, Marckwordt M, Lin R, Jakosky B. (2015).
649 MAVEN SupraThermal and Thermal Ion Composition (STATIC) Instrument. *SPACE SCI*
650 *REV*, 195(1-4), 199-256. doi: 10.1007/s11214-015-0175-6
- 651 19. Mitchell DL, Mazelle C, Sauvaud JA, Thocaven JJ, Rouzaud J, Fedorov A, Rouger P, Toubanc
652 D, Taylor E, Gordon D, Robinson M, Heavner S, Turin P, Diaz-Aguado M, Curtis DW, Lin
653 RP, Jakosky BM. (2016). The MAVEN Solar Wind Electron Analyzer. *SPACE SCI REV*,
654 200(1-4), 495-528. doi: 10.1007/s11214-015-0232-1
- 655 20. Nagy AF, Winterhalter D, Sauer K, Cravens TE, Brecht S, Mazelle C, Crider D, Kallio E,
656 Zakharov A, Dubinin E. (2004). The plasma environment of Mars. *SPACE SCI REV*, 111(1),
657 33-114
- 658 21. Romanelli N, Bertucci C, Gómez D, Mazelle C. (2015). Dependence of the location of the
659 Martian magnetic lobes on the interplanetary magnetic field direction: Observations from Mars
660 Global Surveyor. *Journal of Geophysical Research: Space Physics*, 120(9), 7737-7747. doi:
661 10.1002/2015JA021359
- 662 22. Romanelli N, Gómez D, Bertucci C, Delva M. (2014). STEADY-STATE
663 MAGNETOHYDRODYNAMIC FLOW AROUND AN UNMAGNETIZED CONDUCTING
664 SPHERE. *The Astrophysical Journal*, 789(1), 43. doi: 10.1088/0004-637X/789/1/43
- 665 23. Rong ZJ, Barabash S, Futaana Y, Stenberg G, Zhang TL, Wan WX, Wei Y, Wang XD, Chai
666 LH, Zhong J. (2014). Morphology of magnetic field in near-Venus magnetotail: Venus express
667 observations. *Journal of Geophysical Research: Space Physics*, 119(11), 8838-8847. doi:
668 10.1002/2014JA020461
- 669 24. Rong ZJ, Barabash S, Stenberg G, Futaana Y, Zhang TL, Wan WX, Wei Y, Wang XD. (2015).
670 Technique for diagnosing the flapping motion of magnetotail current sheets based on single-
671 point magnetic field analysis. *Journal of Geophysical Research: Space Physics*, 120(5), 3462-
672 3474. doi: <https://doi.org/10.1002/2014JA020973>
- 673 25. Rong ZJ, Barabash S, Stenberg G, Futaana Y, Zhang TL, Wan WX, Wei Y, Wang XD, Chai
674 LH, Zhong J. (2015). The flapping motion of the Venusian magnetotail: Venus Express

- 675 observations. *Journal of Geophysical Research: Space Physics*, 120(7), 5593-5602. doi:
676 <https://doi.org/10.1002/2015JA021317>
- 677 26. Rong ZJ, Stenberg G, Wei Y, Chai LH, Futaana Y, Barabash S, Wan WX, Shen C. (2016). Is
678 the flow-aligned component of IMF really able to impact the magnetic field structure of
679 Venusian magnetotail? *Journal of Geophysical Research: Space Physics*, 121(11), 10, 910-978,
680 993. doi: 10.1002/2016JA022413
- 681 27. Simon S, Motschmann U. (2009). Titan's induced magnetosphere under non-ideal upstream
682 conditions: 3D multi-species hybrid simulations. *PLANET SPACE SCI*, 57(14-15), 2001-2015.
683 doi: 10.1016/j.pss.2009.08.010
- 684 28. Simon S, van Treeck SC, Wennmacher A, Saur J, Neubauer FM, Bertucci CL, Dougherty MK.
685 (2013). Structure of Titan's induced magnetosphere under varying background magnetic field
686 conditions: Survey of Cassini magnetometer data from flybys TA-T85. *Journal of Geophysical*
687 *Research: Space Physics*, 118(4), 1679-1699. doi: 10.1002/jgra.50096
- 688 29. Sonnerup BU, Scheible M. (1998). Minimum and maximum variance analysis. *Analysis*
689 *methods for multi-spacecraft data*, 1, 185-220
- 690 30. Vignes D, Mazelle C, Rme H, Acuña MH, Connerney JEP, Lin RP, Mitchell DL, Cloutier P,
691 Crider DH, Ness NF. (2000). The solar wind interaction with Mars: Locations and shapes of
692 the bow shock and the magnetic pile-up boundary from the observations of the MAG/ER
693 Experiment onboard Mars Global Surveyor. *GEOPHYS RES LETT*, 27(1), 49-52. doi:
694 10.1029/1999GL010703
- 695 31. Zhang TL, Du J, Ma YJ, Lammer H, Baumjohann W, Wang C, Russell CT. (2009).
696 Disappearing induced magnetosphere at Venus: Implications for close-in exoplanets.
697 *GEOPHYS RES LETT*, 36(20). doi: 10.1029/2009GL040515
- 698